Linked Reactivity at Mineral-Water Interfaces Through Bulk Crystal Conduction

Svetlana V. Yanina and Kevin M. Rosso

Science **320**, 218 (2008);
DOI: 10.1126/science.1154833

Science (print ISSN 0036-8075; online ISSN 1095-9203) is published weekly, except the last week in December, by the American Association for the Advancement of Science, 1200 New York Avenue NW, Washington, DC 20005.

boundary shows maximum Ir concentrations ranging from 0.1 to 87 ng/g in 85 sections from deep marine to continental depositional environments (*4*).
6. J. M. Luck, K. K. Turekian, *Science* **222**, 613 (1983).
7. C. Koeberl, S. B. Shirey, *Palaeogeogr. Palaeoclimatol. Palaeoecol.* **132**, 25 (1997).
8. T. Meisel, U. Krähenbähl, M. A. Nazarov, *Geology* **23**, 313 (1995).
9. R. Frei, K. M. Frei, *Earth Planet. Sci. Lett.* **203**, 691 (2002).
10. D. G. Pearson *et al.*, *Geol. Soc. Am.* **31**, 123 (1999).
11. G. Quitté *et al.*, *Meteorit. Planet. Sci.* **42**, 1567 (2007).
12. B. Peucker-Ehrenbrink, G. E. Ravizza, A. W. Hofmann, *Earth Planet. Sci. Lett.* **130**, 155 (1995).
13. G. Ravizza, B. Peucker-Ehrenbrink, *Science* **302**, 1392 (2003).
14. The marine Os isotope record, like the Ir fluence approach, is not well suited to detecting the impact of differentiated projectiles, such as achondrites with siderophile-element concentrations that are two to three orders of magnitude lower than chondrites (*7*).
15. M. F. Horan, R. J. Walker, J. W. Morgan, J. N. Grossman, A. E. Rubin, *Chem. Geol.* **196**, 5 (2003).
16. J. Whitehead, D. A. Papanastassiou, J. G. Spray, R. A. F. Grieve, G. J. Wasserburg, *Earth Planet. Sci. Lett.* **181**, 473 (2000).
17. Methods and data table are available as supporting material on *Science* Online.
18. The increase in the seawater Os reservoir after an impact event is determined by knowing (i) the Os concentration in modern seawater (~10 pg/kg) (*19*) and (ii) the estimated mass of the seawater (~1.4×10^{21} kg). The product of these gives the mass of Os in the ocean before an impact [mass Os_{sw} (ng)]. The mass of Os derived from the impactor [mass $Os_{impactor}$ (ng)] is $(f/1 - f) \times$ mass Os_{sw}; where $f = (^{187}Os/^{188}Os_{postimpact} - {}^{187}Os/^{188}Os_{preimpact})/(^{187}Os/^{188}Os_{impactor} - {}^{187}Os/^{188}Os_{preimpact})$. The fractional increase in the seawater Os reservoir is (mass Os_{sw} + mass $Os_{impactor}$)/(mass Os_{sw}).
19. S. Levasseur, J.-L. Birck, C. J. Allègre, *Science* **282**, 272 (1998).
20. F. T. Kyte, S. Liu, *Lunar Planet. Sci.* **XXXIII**, 1981 (abstr.) (2002).
21. J. T. Wasson, G. W. Kallemeyn, *Philos. Trans. R. Soc. London Ser. A* **325**, 535 (1988).
22. A doubling of seawater Os concentration to 20 pg/kg would erase the Os deficit.
23. The diameter D is estimated assuming a spherical projectile D (km) = $\{2 \times [\text{mass } Os_{impactor} \times 3/[Os]_{impactor}$ (ng/g) $\times \rho_{impactor}$ (kg/m^3) $\times 4\Pi]^{1/3}\}$/1E4 with mass $Os_{impactor}$ derived from (*18*). $[Os]_{impactor}$ is the Os concentration in the impactor (*21*), and $\rho_{impactor}$ is the density of the impactor (*25*).
24. R. Tagle, P. Claeys, *Geochim. Cosmochim. Acta* **69**, 2877 (2005).
25. R. L. Korotev, Washington Univ. (St. Louis); available at http://meteorites.wustl.edu/id/density.htm.
26. In the calculations (*23*), an Os concentration ($[Os]_{impactor}$) of 490 ng/g (*21*) and an average density ($\rho_{impactor}$) of 3.35 g/cm^3 (*25*) were representative of an L chondrite meteorite (Popigai LEI event), whereas an Os concentration of 807.5 ng/g (*21*) and an averaged density of 3 g/cm^3 (*25*) were used as representative of a carbonaceous chondrite (*28*) for the K-T event.
27. The Ir-based estimate is calculated by knowing the Ir fluence (*3*, *20*), chondritic Ir concentration (Os/Ir = 1.08) (*15*), average density of a chondrite (*25*), and Earth global Ir inventory.
28. F. T. Kyte, *Nature* **396**, 237 (1998).
29. G. S. Collins, K. Wunnemann, *Geology* **33**, 925 (2005).
30. The Ir and Os isotope-based projectile-size estimates probably represent the integrated signal from both the Popigai and the Chesapeake Bay impacts, because spherules believed to derive from both events are found within the single Ir peak at ODP 1090 (*20*). The smaller estimated size for the Chesapeake Bay projectile (*29*) suggests that >90% of the Os and Ir released to the environment was derived from the Popigai event.
31. A. D. Anbar, G. J. Wasserburg, D. A. Papanastassiou, P. S. Andersson, *Science* **273**, 1524 (1996).
32. C.-T. A. Lee, G. J. Wasserburg, F. T. Kyte, *Geochim. Cosmochim. Acta* **67**, 655 (2003).
33. D. S. Ebel, L. Grossman, *Geology* **33**, 293 (2005).
34. In the steady-state, the relation between reservoir size N, removal flux F, and residence time t is $t = N/F$. This relation implies that the Eocene seawater Os concentration was similar to the modern value, because Eocene estimates of Os burial flux (*35*) and Os residence time made in this work are very similar to recent values (*36*–*38*).
35. T. K. Dalai, G. E. Ravizza, B. Peucker-Ehrenbrink, *Earth Planet. Sci. Lett.* **241**, 477 (2006).
36. T. K. Dalai, G. E. Ravizza, *Geochim. Cosmochim. Acta* **70**, 3928 (2006).
37. S. Levasseur, J.-L. Birck, C. J. Allègre, *Earth Planet. Sci. Lett.* **174**, 7 (1999).
38. R. Oxburgh, *Earth Planet. Sci. Lett.* **159**, 183 (1998).
39. K. A. Farley, A. Montanari, E. M. Shoemaker, C. S. Shoemaker, *Science* **280**, 1250 (1998).
40. For example, the lowest K-T boundary $^{187}Os/^{188}Os$ ever reported (0.137) (*8*) corresponds to a projectile size of greater than 6 km in diameter. On the basis of the unusually large Os concentration at this section, we believe that this section does not accurately reflect the true $^{187}Os/^{188}Os$ concentration of seawater immediately after the K-T event. Instead, we suspect a substantial inventory of particulate impact-derived Os.
41. J. W. Morgan, M. F. Horan, R. J. Walker, J. N. Grossman, *Geochim. Cosmochim. Acta* **59**, 2331 (1995).
42. G. S. Collins, H. J. Melosh, R. A. Marcus, *Meteorit. Planet. Sci.* **40**, 817 (2005).
43. F. T. Kyte, *Deep-Sea Res. II* **49**, 1049 (2002).
44. J. E. T. Channell *et al.*, *Geol. Soc. Am. Bull.* **115**, 607 (2003).
45. H. Pälike *et al.*, *Sci. Res.*, *Proc. Ocean Drill. Prog.* (Ocean Drilling Program, College Station, TX, 2005), vol. 199.
46. We thank the ODP for providing the samples, D. Vonderhaar for technical assistance, E. Scott for his advice and expertise on meteorites, and R. Smith for support. Comments by three anonymous reviewers greatly improved the paper. This work was supported by NSF grants OCE and EAR to G.E.R. and B.P.-E.

Supporting Online Material
www.sciencemag.org/cgi/content/full/320/5873/214/DC1
Materials and Methods
SOM Text
Table S1

12 November 2007; accepted 29 February 2008
10.1126/science.1152860

Linked Reactivity at Mineral-Water Interfaces Through Bulk Crystal Conduction

Svetlana V. Yanina and Kevin M. Rosso*

The semiconducting properties of a wide range of minerals are often ignored in the study of their interfacial geochemical behavior. We show that surface-specific charge density accumulation reactions combined with bulk charge carrier diffusivity create conditions under which interfacial electron transfer reactions at one surface couple with those at another via current flow through the crystal bulk. Specifically, we observed that a chemically induced surface potential gradient across hematite (α-Fe_2O_3) crystals is sufficiently high and the bulk electrical resistivity sufficiently low that dissolution of edge surfaces is linked to simultaneous growth of the crystallographically distinct (001) basal plane. The apparent importance of bulk crystal conduction is likely to be generalizable to a host of naturally abundant semiconducting minerals playing varied key roles in soils, sediments, and the atmosphere.

The chemical behavior of mineral-water interfaces is central to aqueous reactivity in natural waters, soil evolution, and atmospheric chemistry and is of direct relevance for maintaining the integrity of waste repositories and remediating environmental pollutants. Traditionally, explorations of fundamental reactions at these interfaces have probed the interaction of water and relevant dissolved ions with crystallographically well-defined mineral surfaces. The pursuit so far has been dominated by the assumption that distinct surfaces of any given crystal behave independently of each other. Except by diffusion through the solution phase or across surface planes, exchange of mass or electron equivalents between sites of differing potential energy at different locations on any given crystal is typically assumed to be negligible. This assumption is nonetheless questionable for the widespread group of minerals that are electrical semiconductors. For example, iron oxides often have moderate to low electrical resistivity (*1*) and have been studied as electrode materials for decades (*2*–*4*). Iron oxide crystal surfaces are chemically reactive with water and ions, leading to solution-dependent charging behavior that differs from one surface type to the next; differing points of zero charge for proton adsorption is but one example (*5*, *6*). This difference should give rise to a surface electric potential gradient ($\Delta\psi_0$) across any crystal that has two or more structurally distinct faces exposed to solution. In principle, this gradient can bias the diffusion of charge carriers (*7*, *8*). Hence, conditions could exist when the gradient across a single crystal is sufficiently large and the electrical resistivity of the material sufficiently

Chemical and Materials Sciences Division, Pacific Northwest National Laboratory, Post Office Box 999, MSIN K8-96, Richland, WA 99352, USA.

*To whom correspondence should be addressed. E-mail: kevin.rosso@pnl.gov

low that interfacial electron transfer reactions at one surface couple with those at another by a current flowing spontaneously through the crystal bulk. The situation is analogous to galvanic metal corrosion, but instead of spatially disordered anodic and cathodic electron transfer sites, the anode and cathode are spatially confined to crystallographically distinct surface planes and are therefore physically separable for measurement. We demonstrate operability of these conditions for iron oxide, uncover their effects on the surface chemical behavior, and make the case that, in nature, different surfaces of certain abundant crystals are inextricably linked.

We examined hematite (α-Fe_2O_3) because it is a wide band gap semiconductor (band gap 1.9 to 2.3 eV) (*1*, *3*) and the most stable form of iron oxide under dry oxidizing conditions; it is extremely common in nature (*9*). It has the corundum structure type based on hexagonal close packed oxygen planes in which 2/3 of the available octahedral cavities are occupied by Fe^{3+}. This structure gives rise to anisotropic electrical resistivity that is higher in the basal plane than along the trigonal axis by up to four orders of magnitude (*10*, *11*); reported bulk resistivities range from 10^2 to 10^6 ohm·m (*1*). When hematite is subjected to oxygen-limited aquatic environments, particularly in acidic conditions, it can be reductively dissolved according to Eq. 1:

$$Fe_2O_3 + 6H^+ + 2e^- \rightarrow 2Fe^{2+}_{(aq)} + 3H_2O \quad (1)$$

which has a standard reduction potential $E° \sim 0.7$ V (*8*, *12*). The fundamental reaction central to the overall process is

$$Fe^{3+}_{(s)} + e^- \rightarrow Fe^{2+}_{(aq)} \quad (2)$$

Sorbed Fe^{2+} from the aqueous phase is capable of reducing hematite Fe^{3+} in this system (*13*–*15*), yielding an iron redox cycle in which no net reduction occurs. Introduction of dicarboxylic acids such as oxalate causes net dissolution by chelating surface Fe^{3+} (ligand assisted dissolution); it also enhances reduction, possibly through the formation of ternary surface complexes with $Fe^{2+}_{(aq)}$, for example (*16*). This collective chemistry is a good test case for our main hypothesis because it involves a source of electron equivalents from Fe^{2+} in solution, a range of potential-determining ions, electron transfer across hematite-solution interfaces, and the possibility of moving electron equivalents through the crystal bulk.

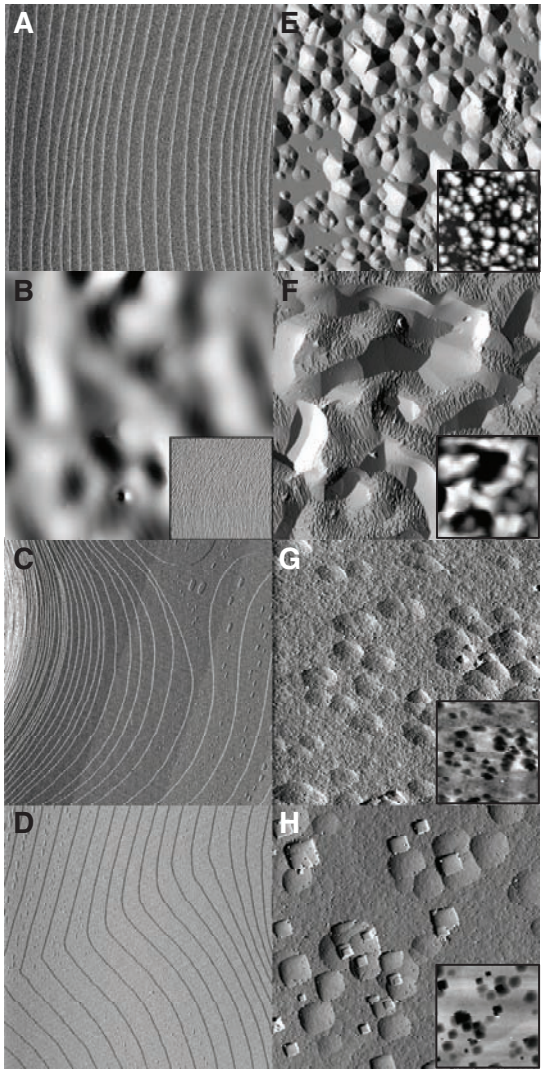

Fig. 1. AFM images of representative hematite surfaces of the natural samples before (**A** to **D**) and after (**E** to **H**) reaction at 75°C for 12 hours in the pH range of 2 to 3 in 1 mM Fe^{2+} and 10 mM oxalate solution free of oxygen. Initial surface morphologies [(A) to (D) 10 μm by 10 μm deflection images] for (A) a (001) surface, (B) a (*hk*0) surface, (C) a (012) surface, and (D) a (113) surface are extremely flat and in all cases except (*hk*0) crystallographically well ordered into terrace-and-step structures at the micrometer scale. At higher resolution [(B) inset, 2 μm by 2 μm deflection image], the (*hk*0) surface is microfaceted with edge terminations. Reacted surfaces [(E) to (H), 20 μm by 20 μm deflection images with corresponding topographic height images in the insets] show a sharp distinction between (E) the (001) surface behavior and (F) the (*hk*0) surface, (G) the (012) surface, and (H) the (113) surface. Large hematite pyramids of uniform orientation nucleate as islands on the initially flat (001) surface (E), achieving average heights of 200 nm and average lateral diameters on the order of a micrometer. In contrast, all other surfaces dissolve. Dissolution of the (*hk*0) surface yields large irregular pits and coarsens the faceted appearance of the surface (F). Dissolution of (012) and (113) surfaces yields large crystallographically controlled etch pits combined with smaller scale roughening [(G) and (H), respectively].

Development of a potential gradient $\Delta\psi_0$ of significant magnitude across the crystal requires selective interaction between potential-determining ions and specific hematite surfaces. We focus here on roles of protons (low pH) and oxalate as a representative dicarboxylic acid. The hematite (001) basal surface is structurally distinct from any edge surfaces. In water, the (001) surface is terminated predominantly by doubly coordinated hydroxyls (*17*–*19*) that are relatively inert to the protonation and deprotonation reactions needed for charge accumulation. Smaller populations of more reactive singly coordinated and triply coordinated hydroxyls, capable of positive charge accumulation, are associated with terminal Fe groups (*19*). Terminal Fe groups with low coordination to the underlying surface can be easily chelated by oxalate anions to form negatively charged mononuclear bidentate inner-sphere surface complexes (*20*, *21*). In contrast, many remaining low-index surfaces of hematite crystals such as (012) are dominated by higher-coordinated Fe (*17*, *22*). This higher-coordinated Fe is more difficult to chelate yet bears singly and/or triply coordinated hydroxyls for charge accumulation. In general therefore, we expect that, relative to other hematite surfaces, the (001) surface should show weaker pH-dependent charge accumulation, an observation increasingly confirmed by recent data and theory (*23*, *24*), and stronger interaction with oxalate anions that increases with decreasing pH.

We performed several experiments to potentiometrically measure $\Delta\psi_0$ for specific hematite surfaces and to determine its effect on their behavior in Fe^{2+} and oxalate solutions. We chose a large natural specular hematite crystal with well-defined surfaces that could be isolated for study. The crystal was low in impurity content (*25*), a natural *n*-type semiconductor (*1*), and had a room temperature electrical resistivity of 10^5 ohm·m as measured by the four-point probe method. Generating replicate samples required cutting specific crystallographic surfaces from the crystal as rectangular prism-shaped specimens, which also yielded a vicinal surface type along cut edges. For example, we prepared millimeter-sized oriented prisms exposing two (001) surfaces on the top and bottom of the prism and four orthogonal (*hk*0) vicinal sides (*25*). Annealing in air under conditions where hematite is the only stable iron oxide effectively cleans and organizes the surfaces without modifying the bulk electrical conductivity. This procedure yields highly organized (001) surfaces, with accompanying (*hk*0) vicinal surfaces that are microfaceted with stable edge terminations (Fig. 1, A and B). Similarly, prism specimens bearing (012) and (113) surfaces (Fig. 1, C and D) with accompanying vicinal surfaces were prepared.

To determine the magnitude of $\Delta\psi_0$ and the roles of Fe^{2+} and oxalate solution components,

we measured the open-circuit potential (E_{OCP}) in four solution types. The E_{OCP} is the electrode rest potential relative to a standard reference electrode. Changes in the E_{OCP} are directly related to changes in ψ_0 (*26*, *27*), which in turn is sensitive to surface complexation reactions with our potential-determining ions H^+, Cl^-, Fe^{2+}, and oxalate species (*28*). The measurements were performed at room temperature at effectively constant ionic strength under anaerobic conditions (*25*). We focused these measurements on the (001) and the accompanying (*hk*0) vicinal surface type. The observed approximately linear pH dependence, with predominantly negative slopes, is consistent with the accumulation of positive surface charge with decreasing pH (Fig. 2). As expected, in pure electrolyte solution the (001) surface showed a less-negative slope relative to that of the (*hk*0) surface, consistent with a lower density of charge accumulation sites on the (001) surface (Fig. 2A). In contrast, oxalate anions bind preferentially to the (001) surface with decreasing pH, even to the point of sign reversal in the slope (Fig. 2B). Addition of Fe^{2+} to either solution shows that its primary effect is to lower the overall potential for both the (001) and (*hk*0) surfaces without substantially modifying the pH dependence (Fig. 2, A and B). Taking $E_{(hk0)} - E_{(001)}$ as an estimate of $\Delta\psi_0$, in the presence of oxalate and irrespective of the presence of $Fe^{2+}_{(aq)}$ we found that the potential gradient is large and positive, on the order of tenths of volts below pH = 3 (Fig. 2C). Under these conditions, we expect that mobile electrons acting as majority carriers in hematite would be directed by $\Delta\psi_0$ from the (001) surface to the (*hk*0) surface. E_{OCP} measurements directly between identical surface types [e.g., $E_{(001)} - E_{(001)}$] (*25*) showed no significant voltage.

To examine the effects of $\Delta\psi_0$ of this sign and magnitude on the surface chemical behavior, we examined surfaces of the oriented prisms from the same sample by using atomic force microscopy (AFM) before and after anaerobic reaction with Fe^{2+}-oxalate solutions. Thermostated batch vessels were used with temperatures ranging from room temperature to 75°C and pH ranging from 2 to 3 (*25*). Fe^{2+}-oxalate concentrations consistent with previously published experiments that establish net dissolution in terms of $Fe^{3+}_{(aq)}$ release on fine-grained powders were used (*16*, *29*, *30*). Collectively, these conditions were selected in keeping with Eq. 1 while also accelerating surface transformations into a more easily observable time frame. Light was excluded in all cases to avoid oxalate acting as a reductant. Equilibrium thermodynamic calculations along with Eh measurements at run conditions confirm that all our reaction conditions lie within the $Fe^{2+}_{(aq)}$ stability field (*25*). Hematite was the limiting reactant; total dissolution would retain undersaturation with respect to any possible iron oxide phases.

AFM examination of (001) surfaces after reaction runs showed remarkable features. In every case, for both natural and synthetic samples, (001) surfaces were overgrown with a hexagonal pseudo-pyramidal morphology of uniform orientation. Images at early stages show the island growth of these features on the initially flat (001) surface (Fig. 1E). After 12 hours, the reaction yielded merged pyramid-covered (001) surfaces with peak-to-valley heights averaging 200 nm and pyramid bases approaching a micrometer in width, imparting a distinct matte appearance to the reacted (001) surface visible to the naked eye. Transmission electron microscopy (TEM) and selected area diffraction measurements along [001] transects of this sample type (fig. S1), along with x-ray photoelectron spectroscopy, x-ray diffraction, and energy dispersive x-ray spectroscopy, confirmed that the grown material is structurally and compositionally α-Fe_2O_3 of identical orientation as the underlying material without detectable impurities. The line of intersection of apparent pyramid "facets" with the (001) plane is consistent with lines of {012}/{001} intersec-

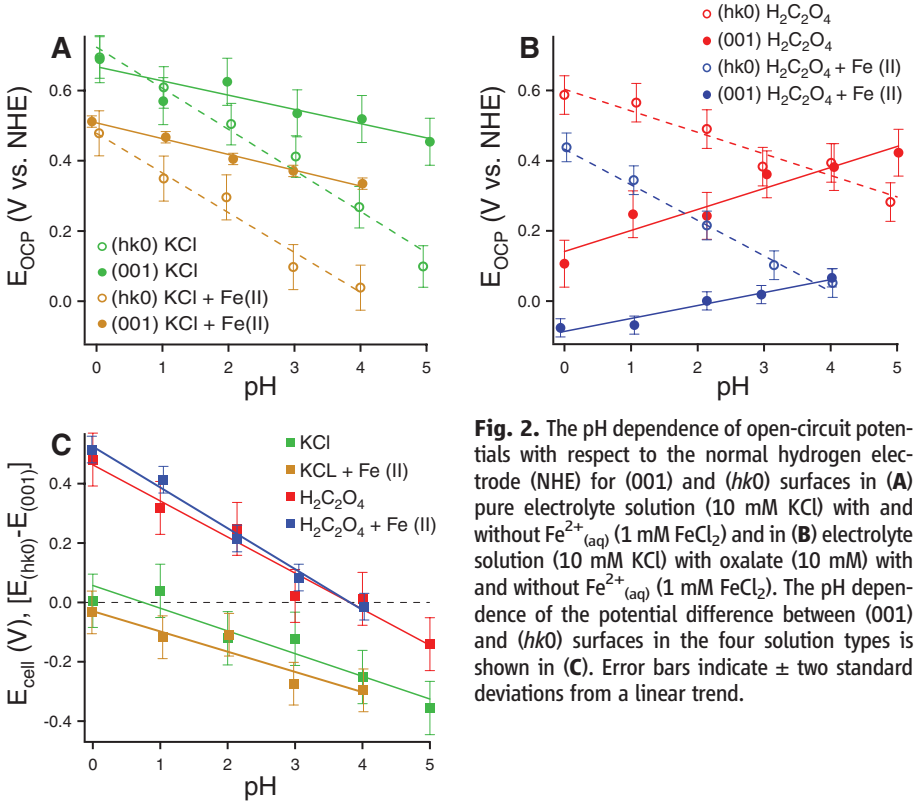

Fig. 2. The pH dependence of open-circuit potentials with respect to the normal hydrogen electrode (NHE) for (001) and (*hk*0) surfaces in (**A**) pure electrolyte solution (10 mM KCl) with and without $Fe^{2+}_{(aq)}$ (1 mM $FeCl_2$) and in (**B**) electrolyte solution (10 mM KCl) with oxalate (10 mM) with and without $Fe^{2+}_{(aq)}$ (1 mM $FeCl_2$). The pH dependence of the potential difference between (001) and (*hk*0) surfaces in the four solution types is shown in (**C**). Error bars indicate ± two standard deviations from a linear trend.

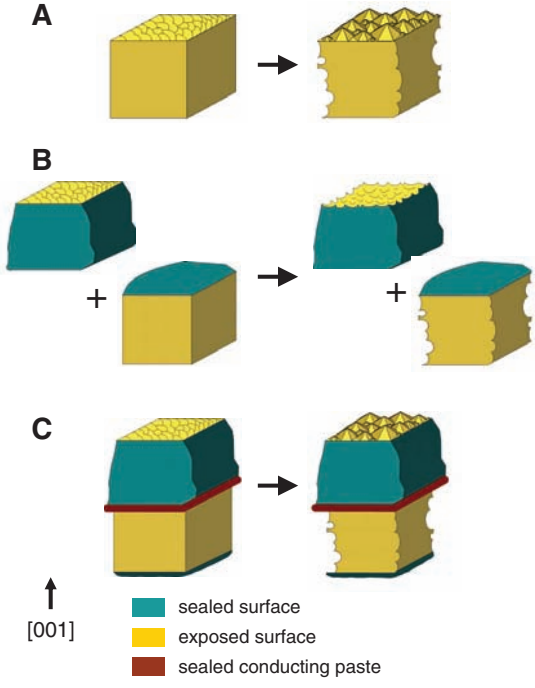

Fig. 3. Schematic diagram summarizing the observed reaction behavior for hematite crystals showing (**A**) (001) pyramidal growth coupled to (*hk*0) dissolution, (**B**) (001) and (*hk*0) dissolution for selectively sealed two-crystal cases where the same surface area and type as in (A) are exposed to solution, and (**C**) (001) pyramidal growth coupled to (*hk*0) dissolution facilitated by a conducting paste connection between two crystals.

tion, but the interplanar angle varies with run duration and does not correspond to low-index planes in hematite. The large size, morphologic symmetry, and mutual orientation of these pyramids require homoepitaxy, that is, growth of additional hematite on hematite.

In contrast, all other surfaces examined show features characteristic of dissolution. For example, the four (*hk*0) vicinal sides of prism samples bearing (001) surfaces on top and bottom exhibited fine-scale pitting and roughening (Fig. 1F). The (012) and (113) surfaces of prism samples show development of etch pits at various length scales and with symmetry corresponding to crystallographic orientation (Fig. 1, G and H). We observed identical behavior under the same conditions with use of synthetic tabular hematite crystals bearing primarily (001) and (012) surfaces, in which case no surface preparation by annealing was required (fig. S2). The conclusion is that the hematite (001) surface grows under our conditions whereas all other surfaces sampled dissolve, as represented schematically in Fig. 3A.

We designed experiments using the prism samples to test whether or not pyramid islands are deposited on the (001) surface by precipitation of trace Fe^{3+} from solution (*16*). In these experiments, two prism samples were used in the reaction vessel instead of one. Four (*hk*0) vicinal sides of one crystal were sealed with an inert epoxy (*25*), leaving two (001) surfaces exposed, whereas on the other crystal the two (001) surfaces were sealed, leaving four vicinal surfaces exposed. Collectively, the two crystals expose the same six kinds of surfaces to solution as in the runs above with one crystal, in the same relative proportion and surface area, but they involve (001) surfaces that are physically separated from the (*hk*0) surfaces (Fig. 3B). In this case, the results of reaction runs show only dissolution features on all exposed surfaces, including (001) (fig. S3A). The (001) pyramidal morphology does not develop in this separated two-crystal configuration. The same experiment performed on samples in which the pyramidal morphology had already been grown on (001) before sealing its (*hk*0) sides showed dissolution of the pyramidal overgrowths on the (001) surface (fig. S3B). Therefore, the (001) pyramidal overgrowths do not form by precipitation of ferric iron. Furthermore, we deduce that chemical processes at the (001)-solution interface causing pyramidal growth during reaction are facilitated by solid contact between the (001) and (*hk*0) surfaces; that is, these surfaces must be on the same crystal.

The behavior strongly suggests that bulk charge transport provides the link between the two types of surfaces. As a further test, we again prepared two crystals with partial exposure of (001) on one and (*hk*0) surfaces on the other, except this time with an electrical connection between them (Fig. 3C). A crystal exposing only (001) surfaces was connected to a crystal beneath exposing only (*hk*0) surfaces by electrically conductive colloidal Ag paste, which was subsequently cured, sealed off from contact with solution using additional epoxy, and tested for ohmic behavior by resistivity measurements. In this design, the crystals are effectively wired together by the (001)-Ag-(001) junction between them. Reaction in this wired two-crystal configuration proceeds as if the crystals were one; pyramidal hematite grows on the exposed (001) surface of the upper crystal (fig. S3C), whereas the four (*hk*0) sides of the lower crystal dissolve (Fig. 3C). Therefore, the nature of the interaction between the (001) and vicinal surfaces that gives rise to the pyramidal growth of hematite (001) during reaction derives from bulk charge transport. Surface diffusion along the hematite-solution interface was ruled out by painting a ring of sealant on a (001) surface so that only bulk transport could access the circumscribed region, and within that region hematite island growth also occurred (fig. S4).

The collective behavior of the system is therefore suggestive of two distinct but coupled interfacial processes: growth at (001) by

$$Fe^{2+}_{(aq)} \rightarrow Fe^{2+}_{(001)} \rightarrow Fe^{3+}_{(001)} + e^- \quad (3)$$

and dissolution of edge surfaces, for example, (*hk*0) surfaces, by

$$Fe^{3+}_{(hk0)} + e^- \rightarrow Fe^{2+}_{(hk0)} \rightarrow Fe^{2+}_{(aq)} \quad (4)$$

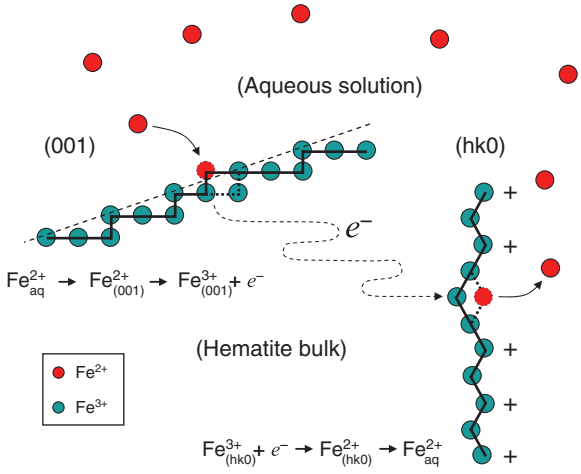

Fig. 4. Schematic diagram depicting the inferred coupled interfacial electron transfer process operative under our conditions for the hematite single crystals. The chemically self-induced surface potential gradient across the crystal directs current flow through the bulk. The current is facilitated by sufficiently low electrical resistivity in a process that is fed by net injection of electron equivalents at (001) surfaces and net release of electron equivalents at (*hk*0) surfaces.

with coupling mediated by charge transport from (001) to (*hk*0) surfaces through the crystal bulk. The process involves preferential net oxidative adsorption of $Fe^{2+}_{(aq)}$ at the (001)-solution interface and valence interchange with structural Fe^{3+} at that surface (Fig. 4). At temperatures of interest (room temperature and higher), bulk charge transport is sufficiently facile to support a small current through the bulk. Net electron equivalents injected into the (001) surface follow an electrically biased random walk through the crystal to (*hk*0) surfaces. At (*hk*0) exit points, internal reduction of Fe^{3+} to Fe^{2+} solubilizes and releases iron into solution. This circuit is driven by the $\Delta\psi_0$ gradient generated across the crystal from divergent charge accumulation at structurally distinct surface types. The sign and magnitude of $\Delta\psi_0$, the conductivity of the natural crystal, and the growth rates of the pyramidal islands are all mutually consistent. For example, taking $\Delta\psi_0 = 0.2$ V at pH = 2, a temperature-adjusted electrical resistivity = 10^4 ohm·m for 75°C (*31*, *32*), and an electron transport path length of 1 mm, the maximum amount of additional hematite expected on the (001) surface in 12 hours is a layer ~100 nm thick, the same order of magnitude as that observed. Surface potential–driven charge carrier diffusivity has been invoked qualitatively to explain microscopic oxide transformation processes before (*13*, *33*, *34*) but not on the length scale examined here nor with surface specificity. Given the observation that the (001) surface continues to grow beyond the coalescence of the pyramidal islands, at the atomic scale the pyramidal (001) morphology must retain the essential structural and therefore chemical characteristics that give rise to the potential of the initial (001) surface. Furthermore, the observed process does not preclude traditionally held spatially localized dissolution in the hematite system. Rather, the evidence suggests that the processes operate in parallel and that the behavior based on the electrical circuit through the crystal dominates when chemical requirements that establish a large enough surface electric potential gradient are met.

The finding provides insight into the reductive transformation of iron oxides, which is important in the biogeochemical cycling of iron in nature and the removal of iron oxide films in industry. Because this finding can be easily generalized to a host of naturally abundant semiconducting transition metal oxide and sulfide minerals capable of dominating the interfacial surface area in soils, sediments, and among atmospheric particles, its implications are fairly widespread. Of immediate impact is the concept that the reactivity of any given surface on such materials can be coupled to that of another surface, with a dependence on crystal morphology as a whole. This phenomenon should apply to natural crystals in the environment as well as those selectively cut, broken, or otherwise prepared for laboratory study.

References and Notes

1. R. T. Shuey, *Semiconducting Ore Minerals*, vol. 4 of *Developments in Economic Geology* (Elsevier, Amsterdam, 1975).
2. J. H. Kennedy, K. W. Frese, *J. Electrochem. Soc.* **125**, 723 (1978).
3. C. Gleitzer, J. Nowotny, M. Rekas, *Appl. Phys. A Mat. Sci. Proc.* **53**, 310 (1991).
4. B. A. Balko, K. M. Clarkson, *J. Electrochem. Soc.* **148**, E85 (2001).
5. P. Venema, T. Hiemstra, P. G. Weidler, W. H. van Riemsdijk, *J. Colloid Interface Sci.* **198**, 282 (1998).
6. F. Gaboriaud, J. Ehrhardt, *Geochim. Cosmochim. Acta* **67**, 967 (2003).
7. C. G. B. Garrett, W. H. Brattain, *Phys. Rev.* **99**, 376 (1955).
8. P. Mulvaney, V. Swayambunathan, F. Grieser, D. Meisel, *J. Phys. Chem.* **92**, 6732 (1988).
9. R. M. Cornell, U. Schwertmann, *The Iron Oxides: Structure, Properties, Reactions, Occurrence and Uses* (VCH, Weinheim, Germany, 2003).
10. T. Nakau, *J. Phys. Soc. Jpn.* **15**, 727 (1960).
11. N. Iordanova, M. Dupuis, K. M. Rosso, *J. Chem. Phys.* **122**, 144305 (2005).
12. J. S. LaKind, A. T. Stone, *Geochim. Cosmochim. Acta* **53**, 961 (1989).
13. P. Mulvaney, R. Cooper, F. Grieser, D. Meisel, *Langmuir* **4**, 1206 (1988).
14. A. G. B. Williams, M. M. Scherer, *Environ. Sci. Tech.* **38**, 4782 (2004).
15. P. Larese-Casanova, M. M. Scherer, *Environ. Sci. Tech.* **41**, 471 (2007).
16. D. Suter, C. Siffert, B. Sulzberger, W. Stumm, *Naturwissenschaften* **75**, 571 (1988).
17. V. Barron, J. Torrent, *J. Colloid Interface Sci.* **177**, 407 (1996).
18. C. M. Eggleston *et al.*, *Geochim. Cosmochim. Acta* **67**, 985 (2003).
19. T. P. Trainor *et al.*, *Surf. Sci.* **573**, 204 (2004).
20. O. W. Duckworth, S. T. Martin, *Geochim. Cosmochim. Acta* **65**, 4289 (2001).
21. T. H. Yoon, S. B. Johnson, C. B. Musgrave, G. E. Brown, *Geochim. Cosmochim. Acta* **68**, 4505 (2004).
22. J. R. Rustad, E. Wasserman, A. R. Felmy, *Surf. Sci.* **424**, 28 (1999).
23. T. Hiemstra, W. H. Van Riemsdijk, *Langmuir* **15**, 8045 (1999).
24. P. Zarzycki, *Appl. Surf. Sci.* **253**, 7604 (2007).
25. Materials and methods are available on *Science* Online.
26. M. J. Avena, O. R. Camara, C. P. Depauli, *Colloid Surf.* **69**, 217 (1993).
27. N. Kallay, T. Preocanin, *J. Colloid Interface Sci.* **318**, 290 (2008).
28. J. A. Davis, R. O. James, J. O. Leckie, *J. Colloid Interface Sci.* **63**, 480 (1978).
29. B. Zinder, G. Furrer, W. Stumm, *Geochim. Cosmochim. Acta* **50**, 1861 (1986).
30. S. Banwart, S. Davies, W. Stumm, *Colloid Surf.* **39**, 303 (1989).
31. S. Kerisit, K. M. Rosso, *Geochim. Cosmochim. Acta* **70**, 1888 (2006).
32. S. Kerisit, K. M. Rosso, *J. Chem. Phys.* **127**, 124706 (2007).
33. N. M. Dimitrijevic, D. Savic, O. I. Micic, A. J. Nozik, *J. Phys. Chem.* **88**, 4278 (1984).
34. J. P. Jolivet, E. Tronc, *J. Colloid Interface Sci.* **125**, 688 (1988).
35. This research was supported by the U.S. Department of Energy (DOE), Office of Basic Energy Sciences, Geosciences Program. It was performed at the William R. Wiley Environmental Molecular Sciences Laboratory (EMSL) at the Pacific Northwest National Laboratory (PNNL). The EMSL is funded by the DOE Office of Biological and Environmental Research. PNNL is operated by Battelle for the DOE under contract DE-AC06-76RLO 1830. We gratefully acknowledge the assistance of C. Wang for TEM; B. Arey for scanning electron microscopy; D. McCready for pole reflection x-ray diffraction; Y. Lin for access to electrochemistry apparatus; and A. Felmy, E. Ilton, and J. Amonette for comments on an early version of this manuscript.

Supporting Online Material

www.sciencemag.org/cgi/content/full/1154833/DC1
Materials and Methods
Figs. S1 to S4
References

4 January 2008; accepted 25 February 2008
Published online 6 March 2008;
10.1126/science.1154833
Include this information when citing this paper.

Aligning Conservation Priorities Across Taxa in Madagascar with High-Resolution Planning Tools

C. Kremen,[1,2]*† A. Cameron,[1,2]† A. Moilanen,[3] S. J. Phillips,[4] C. D. Thomas,[5] H. Beentje,[6] J. Dransfield,[6] B. L. Fisher,[7] F. Glaw,[8] T. C. Good,[9] G. J. Harper,[10] R. J. Hijmans,[11] D. C. Lees,[12] E. Louis Jr.,[13] R. A. Nussbaum,[14] C. J. Raxworthy,[15] A. Razafimpahanana,[2] G. E. Schatz,[16] M. Vences,[17] D. R. Vieites,[18] P. C. Wright,[19] M. L. Zjhra[9]

Globally, priority areas for biodiversity are relatively well known, yet few detailed plans exist to direct conservation action within them, despite urgent need. Madagascar, like other globally recognized biodiversity hot spots, has complex spatial patterns of endemism that differ among taxonomic groups, creating challenges for the selection of within-country priorities. We show, in an analysis of wide taxonomic and geographic breadth and high spatial resolution, that multitaxonomic rather than single-taxon approaches are critical for identifying areas likely to promote the persistence of most species. Our conservation prioritization, facilitated by newly available techniques, identifies optimal expansion sites for the Madagascar government's current goal of tripling the land area under protection. Our findings further suggest that high-resolution multitaxonomic approaches to prioritization may be necessary to ensure protection for biodiversity in other global hot spots.

Approximately 50% of plant and 71 to 82% of vertebrate species are concentrated in biodiversity hot spots covering only 2.3% of Earth's land surface (*1*). These irreplaceable regions are thus among the highest global priorities for terrestrial conservation; reasonable consensus exists on their importance among various global prioritization schemes that identify areas of both high threat and unique biodiversity (*2*). The spatial patterns of species richness, endemism, and rarity of different taxonomic groups within priority areas, however, rarely align and are less well understood (*3*–*6*). Detailed analysis of these patterns is required to allocate conservation resources most effectively (*7*, *8*).

To date, only a few quantitative, high-resolution, systematic assessments of conservation priorities have been developed within these highly threatened and biodiverse regions (*9*, *10*). This deficiency results from multiple obstacles, including limited data or access to data on species distributions and computational constraints on achieving high-resolution analyses over large geographic areas. We have been able to overcome each of these obstacles for Madagascar, a global conservation priority (*1*, *2*, *11*). Like many other regions (*3*–*6*), Madagascar has complex, often nonconcordant patterns of microendemism among taxa (*12*–*17*), rendering the design of efficient protected-area networks particularly difficult (*4*, *6*). We collated data for endemic species in six major taxonomic groups [ants, butterflies, frogs, geckos, lemurs, and plants (table S1)], using recent robust techniques in species distribution modeling (*18*, *19*) and conservation planning (*20*, *21*) to produce the first quantitative conservation prioritization for a biodiversity hot spot with this combination of taxonomic breadth (2315 species), geographic extent (587,040 km^2), and spatial resolution (30–arc sec grid = ~0.86 km^2).

Currently, an important opportunity exists to influence reserve network design in Madagascar, given the government's commitment, announced at the World Parks Congress in 2003, to triple its existing protected-area network to 10% coverage (*22*). Toward this goal, our high-resolution analysis prioritizes areas by their estimated contribution to the persistence of these 2315 species and identifies regions that optimally complement the existing reserve network in Madagascar.

We input expert-validated distribution models for 829 species and point occurrence data for the remaining species [those with too few occurrences to model, called rare target species (RTS)] into a prioritization algorithm, Zonation (*20*, *21*), which generates a nested ranking of conservation priorities (*23*). Species that experienced a large proportional loss of suitable habitat (range reduction) between the years 1950 and 2000 were given higher weightings [equation 2 of (*23*), (*24*)]. We evaluated all solutions [defined here as the highest-ranked 10% of the landscape to match the target that Madagascar has set for conservation (*22*)] in two ways: (i) percent of species entirely